Thin Solid Films 700 (2020) 137916

Contents lists available at ScienceDirect

Thin Solid Films

journal homepage: www.elsevier.com/locate/tsf

Origin of enhanced carrier mobility and electrical conductivity in seed-layer assisted sputtered grown Al doped ZnO thin films

Naveen Kumar[a], Ashraful Haider Chowdhury[b], Behzad Bahrami[b], Mamun Reza Khan[b], Qiquan Qiao[b], Mukesh Kumar[a,*]

[a] Functional and Renewable Energy Materials Laboratory, Indian Institute of Technology Ropar, Punjab, 140001, India
[b] Department of Electrical Engineering and Computer Science, South Dakota State University, Brookings, USA

ARTICLE INFO

Keywords:
Transparent conducting oxide
Aluminium-doped zinc oxide
Hall mobility
Seed layer
Defects
Kelvin probe force microscopy

ABSTRACT

In the present study, a ZnO seed-layer assisted sputtered deposition approach is used to enhance the carrier mobility and electrical conductivity of Al doped ZnO (AZO) thin film. The seed layer assisted grown AZO thin film showed an electrical conductivity, optical transmittance, and high figure-of-merit of 1806.94 ± 10.50 S/cm, >90% (Vis-NIR), and 1.68 × 10^{-2} Ω^{-1}, respectively. This high optoelctronic properties make AZO thin film qualified to be used for transparent electrode applications. The carrier mobility in the seed-layer assisted grown AZO thin film is observed to be 15.21 ± 0.04 cm^2/Vs which is two-fold higher than AZO thin film grown without seed-layer. The origin of enhanced carrier mobility is investigated in the light of generated defects and their nanoscale distribution in the polycrystalline AZO thin film during the sputtering process. The low grain boundary potential is observed in seed layer assisted grown AZO thin film using nanoscale Kelvin probe force microscopy and was attributed to the low defects segregation towards grain boundaries. The argument of low carrier defects like zinc interstitial and oxygen vacancies in seed-layer assisted grown AZO thin film is experimentally verified using X-ray photoelectron spectroscopy analysis. The analysis of defect chemistry and their nanoscale distribution helps us to understand that intrinsic defects and their segregation at grain boundaries critically affect the carrier mobility in AZO thin film.

1. Introduction

Transparent conducting oxides (TCOs) are the wide band gap materials (Eg > 3 eV) and show high electrical conductivity (~10^3–10^4S/cm) and high optical transmittance (>85%) in Vis-NIR region. This idiosyncratic property makes TCO usable in flat panel display, light emitting diodes, electrochromic windows, photovoltaic devices, and thin film transistors [1–6]. Sn doped In_2O_3 (ITO) is considered an industrially standard TCO due to its remarkable optoelectronic properties [7–10]. However, the scarcity and high cost of indium (In) in ITO have necessitated the need to find In-free TCO having the potential to replace ITO. Earth abundant Al doped ZnO (AZO) is the most preferable TCO to be used in optoelectronic devices, however, despite having high optical transmittance, the low carrier mobility is being considered a well-known challenge to enhance the electrical conductivity without compromising the optical transmittance window [11–14]. The electrical properties of AZO thin films were found strongly dependent on the grain size, defect generation, and their segregation towards grain boundaries [15–17]. The thickness-dependent electrical properties of AZO thin film were investigated and defects were correlated with the thickness of the growing film [18,19]. Tseng et al. have studied the effect of AZO film thickness with its electrical, optical and structural properties and achieved maximum carrier mobility for the thickness more than 600 nm [15]. Many other reports have also shown that the electrical properties of AZO thin film are critically decided by the thickness of the grown film [20–22]. However, in all these reports, the dependency of electrical properties on the thickness of the film was correlated indirectly to the change in structural property and defect chemistry of grown AZO thin film. In an alternative approach, controlled plasma chemistry during the sputtering process using Radio Frequency (RF) superimposed Direct Current (DC) sputtering is used to improve the carrier mobility [16]. Kumar et al. have deposited AZO thin films using RF superimposed DC sputtering by controlled plasma chemistry and a substantial improvement in carrier mobility was observed at RF/(RF + DC) of 75% [23]. Similarly, improved optoelectronic properties of AZO thin film using RF superimposed DC sputtering for other oxides e.g., In-Zn-O, In-Sn-O, and Ga-Zn-O are reported [24–26]. However, tuning of RF/(RF + DC) growth parameters alter the energy

* Corresponding author.
E-mail address: mkumar@iitrpr.ac.in (M. Kumar).

https://doi.org/10.1016/j.tsf.2020.137916
Received 20 May 2019; Received in revised form 24 February 2020; Accepted 1 March 2020
Available online 02 March 2020
0040-6090/

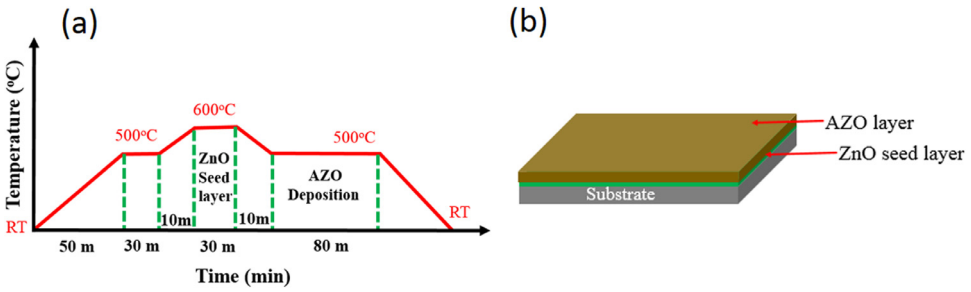

Fig. 1. (a) Temperature profile to deposit AZO thin film with the ZnO seed layer and (b) schematic of ZnO seed layer assisted AZO thin film.

Table 1
The electrical properties of AZO thin film deposited for different thicknesses of the ZnO seed layer of 20, 30, 40, and 50 nm.

Thickness (nm)	Electrical resistivity (Ω cm)	Hall mobility (Cm^2/Vs)	Carrier density (cm^{-3})
20	(2.79 ± 0.04) × 10^{-3}	7.17 ± 0.07	(3.12 ± 0.03) × 10^{20}
30	(2.43 ± 0.01) × 10^{-3}	9.23 ± 0.01	(2.79 ± 0.01) × 10^{20}
40	(5.54 ± 0.03) × 10^{-4}	15.21 ± 0.04	(7.42 ± 0.02) × 10^{20}
50	(4.67 ± 0.09) × 10^{-3}	4.31 ± 0.15	(3.11 ± 0.05) × 10^{20}

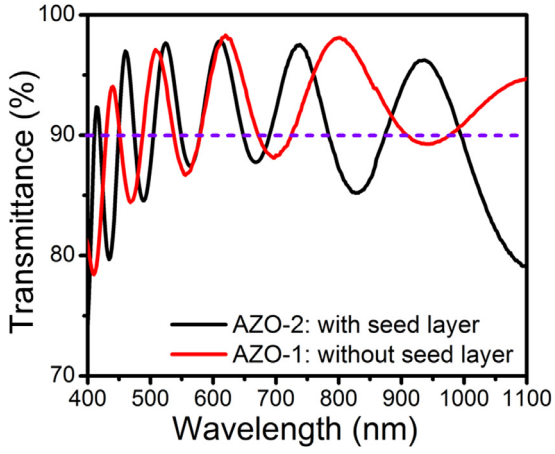

Fig. 2. Optical transmittance spectra of AZO thin films deposited without (AZO-1) and with the ZnO seed layer (AZO-2).

and flux of high energetic ions in the plasma and result in high residual stress in the grown thin film which is not desirable for next generation flexible devices [24,27]. The grain size and associated defects with the thickness and plasma chemistry were found to control the electrical properties of AZO thin film but none of the reports have studied the type of defects and their distribution in AZO thin film or effect of the seed layer. Recently Kanika et al. have shown the importance of the Ga_2O_3 seed layer for the deposition of a better quality of Ga_2O_3 film for UV blind photodetectors [28]. No study of the ZnO seed layer effect on the optoelectronic properties of AZO thin films is reported so far. The study to control the defects and their nanoscale distribution in grain and grain boundary may critically affect the carrier scattering and requires to correlate the processing condition and optoelectronic properties of AZO thin film for their usage in next generation optoelectronic devices.

In this work, seed layer assisted grown AZO thin film shows two-fold enhanced carrier mobility in contrast to those grown without a seed layer. All AZO thin films showed a polycrystalline structure with nearly equal crystallite size. To understand the origin of enhanced carrier mobility, the generated defects, and their nanoscale distribution are investigated using X-ray Photoelectron Spectroscopy (XPS), nanoscale Kelvin Probe Force Microscopy (KPFM) and Conducting Atomic Force Microscopy (CAFM). The XPS results show low defects like zinc interstitial and oxygen vacancies in seed-layer assisted grown AZO thin films. The KPFM and CAFM results reveal the formation of low grain boundary potential and uniform surface current in seed layer assisted grown AZO thin film, respectively. The results reveal that low defects and their segregation at grain boundaries lead to reduced carrier scattering and enhanced carrier mobility in seed layer-assisted grown AZO thin films.

2. Experimental and characterization details

The AZO thin films are deposited by using the mixed ceramic target of 2 wt% Al_2O_3 and 98 wt% ZnO target (K. J. Lesker) on the Corning EAGLE XG glass substrate. Before deposition, the glass substrates are cleaned in deionized water and soap solution followed by sonication for 30 min in acetone and propanol. The cleaned substrates are UV cured

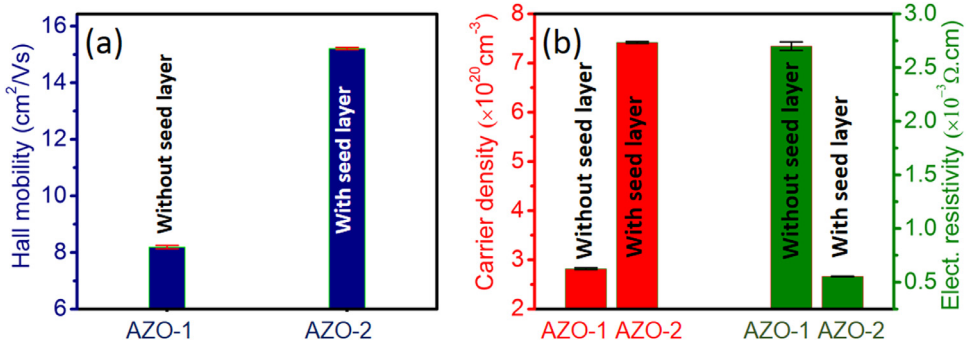

Fig. 3. (a) Hall mobility and (b) carrier concentration and electrical resistivity of AZO thin film deposited without (AZO-1) and with seed layer (AZO-2).

Table 2
Comparison between electrical conductivity and figure of merit of AZO thin films with reported literature and present work.

S. No	TCO thin film Structure	Growth Technique	Electrical conductivtiy (S/cm)	Figure of Merit (FOM)(Ω^{-1})	Ref
1	AZO thin film	Sol-gel	2.34	6.27×10^{-8}	[29]
2	AZO thin film	Sputtering	1400.56	NA	[33]
3	AZO thin film	Sputtering	286.45	NA	[34]
4	AZO thin film	Sputtering	1497.00	1.11×10^{-2}	[35]
5	Hydrogen doped AZO	Chemical	1152.07	NA	[36]
6	AZO thin film	Chemical	101.01	NA	[37]
7	Cr coated AZO thin film	Sputtering	35.76	NA	[38]
8	AZO thin film	ALD	833.33	NA	[39]
9	AZO thin film	Sputtering	1000.00	NA	[40]
10	AZO thin film	Sputtering	833.33	NA	[41]
11	AZO/Ag/AZO	Sputtering	NA	1.79×10^{-3}	[31]
12	AZO/Ag/AZO	Sputtering	NA	9.00×10^{-3}	[42]
13	AZO/Ga/AZO	Sputtering	NA	9.50×10^{-4}	[32]
14	AZO/AgNW/AZO	Sputtering	NA	4.1×10^{-3}	[43]
15	AZO thin film	sputtering	1806.94 ± 10.50	1.68×10^{-2}	Present work

for 30 min and loaded into the high vacuum sputtering chamber. The vacuum chamber is pumped down to the base pressure of 1.1×10^{-4} Pa (8×10^{-7} Torr). The Ar gas of flow rate of 50 SCCM is used to maintain the deposition pressure of 6.7×10^{-1} Pa (5 mTorr). The AZO thin films are deposited at 100 W RF power and 6.7×10^{-1} Pa (5 mTorr) sputtering pressure with and without the ZnO seed-layer. To deposit AZO thin film with the ZnO seed layer, the AZO and ZnO targets are mounted in the confocal arrangement in the sputtering chamber features two sputtering guns equipped with the separate gun shutters to cover the other target if it is not being used. The vacuum of the chamber is not broken and the ZnO seed layer assisted AZO thin film is deposited in one go using temperature profile shown in Fig. 1(a). A ZnO seed layer of 40 ± 10 nm thickness is deposited at 600 °C at 50 W RF power followed by the deposition of AZO thin film of 200 ± 20 nm thickness at 500 °C. The thickness of both AZO thin film without and with the ZnO seed layer ($t_{ZnO} + t_{AZO}$) is kept almost the same ~250 nm by varying the deposition time. The temperature profile and schematic of the ZnO seed layer assisted AZO thin film are shown in Figs. 1(a) and (b), respectively. The AZO thin film without the ZnO seed layer is grown at 500 °C under identical conditions.

AZO thin film deposited without the ZnO seed layer is named as AZO-1 and with the ZnO seed layer is named as AZO-2. The thickness of AZO thin films is measured and verified with quartz crystal monitor and Atomic Force Microscopy (AFM), respectively. The AZO thin films were also deposited with different thicknesses of the ZnO seed layer of 20, 30, and 50 nm. Among different thicknesses of the ZnO seed layer, the 40 nm of the ZnO seed layer has shown better electrical properties of AZO thin film, therefore, 40 nm of ZnO seed layer is chosen for further experiment. The electrical properties of the AZO thin film deposited with different thicknesses of the ZnO seed layer are shown in Table 1.

The optical properties of AZO thin films are measured by the Perkin Elmer lambda 950 UV/Vis spectrophotometer. The optical transmittance is measured with respect to the Corning EAGLE XG glass substrate. The electrical properties of AZO thin films are studied by the ezHems Nanomagnetics Hall measurements system with the magnetic field of 1 Tesla at room temperature. For electrical properties measurements, a glass substrate of 1 cm × 1 cm area is used. Structural analysis is done with Rigaku smartlab X-ray diffractometer. The PhotonMax high-flux 9 kW rotating anode X-ray source coupled with a HyPix-3000 high-energy-resolution 2D multidimensional semiconductor detector is used to record the XRD pattern. The KPFM is measured using Agilent 5500 multimode scanning probe microscopy system. Multi75E-G budget sensor with Cr/Pt coating tip having a resonance frequency of 75 kHz and a force constant of 3 N m^{-1} is used for KPFM measurements. The first resonance frequency of 67 kHz is fed into the first lock-in amplifier (L1A1) and the second resonance frequency of 5 kHz is fed into the second lock-in amplifier (L1A2). The separation between tip and sample is controlled by the L1A1 to do topographic and phase imaging while L1A2 is used for surface potential measurements. LIA2 provides an electrical oscillation to the tip at 5 kHz with a dc offset of −3 V and the drive percentage of LIA2 was approximately 15% to attain a surface potential amplitude of 0.2 V. The AC/DC bias voltage is applied to the sample during the KPFM measurements. Surface potential vs. z scan is performed to avoid the interference of surface topography into the KPFM signal. CAFM measurements are performed in contact mode using a Cr/Pt coated Si tip (Budget Sensors ContE-G; tip radius 20 nm; force constant of 0.2 N m^{-1}; resonance frequency of 13 kHz) with 4 V sample bias. For defects and chemical composition, XPS measurements are performed using Thermo Fisher scientific ESCALAB Xi+ model using Al K_α source with the energy of 1486.6 eV. The AZO films are pre-sputtered with Ar ions of 1 KeV beam energy. The sample current is kept 1μA. Initially, the chamber is pumped down to the base pressure of 5×10^{-8} Pa. Later, for charge neutralization and sample cleaning, Ar gun is introduced inside the chamber which reduces the base pressure to ~5×10^{-6} Pa. For deconvoluting and fitting the XPS peaks, "XPS PEAK 41" software is used. All the peaks fitting are done with Shirley background.

3. Results and discussion

The optical transmittance of AZO thin film without the ZnO see layer (AZO-1) and with the ZnO seed layer (AZO-2) is shown in Fig. 2. AZO thin films showed ~90% transmittance in Vis to NIR region. The formation of fringes in transmittance spectra is due to the interference formation of light from different interfaces. The optical band gap of AZO-1 and AZO-2 was also calculated using the Tauc plot and found 3.26 eV and 3.38 eV, respectively.

The electrical properties of AZO thin films deposited without the ZnO seed layer (AZO-1) and with the ZnO seed layer (AZO-2) are shown in Fig. 3. The Hall mobility, electrical resistivity, and carrier density of AZO thin film deposited without seed layer (AZO-1) were 8.19 ± 0.06 cm^2/Vs, (2.70 ± 0.04) × 10^{-3} Ω cm, and (2.82 ± 0.02) × 10^{20} cm^{-3}, respectively. When the AZO thin film is deposited over the ZnO seed layer, the electrical properties of AZO are enhanced drastically. The Hall mobility, electrical resistivity, and carrier density of AZO thin film were 15.21 ± 0.04 cm^2/Vs, (5.54 ± 0.03) × 10^{-4} Ω cm, and (7.42 ± 0.02) × 10^{20} cm^{-3}, respectively. Fig. 3(a) shows the variation in Hall mobility in AZO thin film without and with ZnO seed layer incorporation.

Hall mobility is found nearly double after depositing AZO thin film with the ZnO seed layer. Fig. 3(b) shows the variation of carrier density and the electrical resistivity of AZO thin film without and with the ZnO

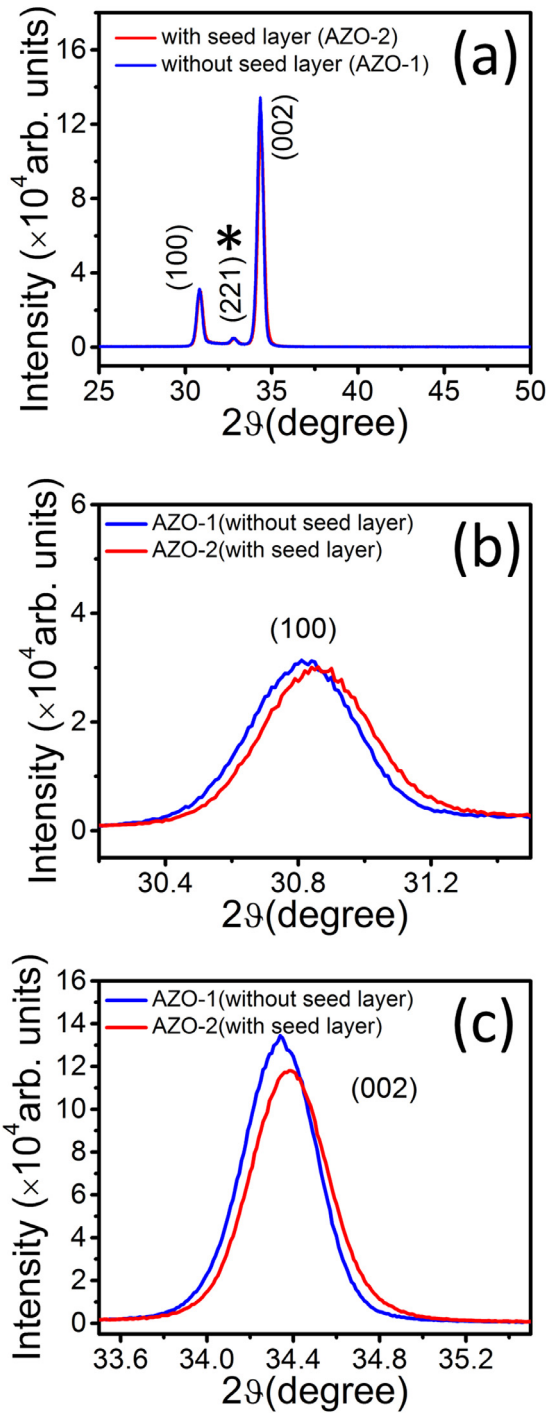

Fig. 4. (a) XRD pattern of AZO thin films without seed layer (AZO-1) and with seed layer (AZO-2) deposited on the corning glass [* (221) peak corresponds to the Al2O3 peak]. (b) and (c) are the XRD pattern that show the (100) and (002) peak shifts in AZO-1 and AZO-2 thin films, respectively.

seed layer. It is important to note that the electrical conductivity of AZO thin film deposited with the seed layer is enhanced by five-fold and reached the value of 1806.94 ± 10.50 S/cm which is more than the minimum conductivity requirement for any TCO material to be used for optoelectronic applications. The increase in conductivity is attributed to the improved mobility and high carrier density in AZO-2 thin film. Moreover, the increase in the optical band gap of AZO-2 can be attributed to the Burstein Moss effect due to the high carrier density of AZO-2 than AZO-1 thin film. The free carriers may occupy the lowest conduction band minima sates that may increase the energy separation of available optical transition level from valence band maxima to conduction band minima and subsequently increases the optical band gap of AZO-2. Along with high electrical conductivity, high optical transmittance is also considered for figure-of-merit (FOM) of TCO materials. FOM is also calculated for AZO thin film deposited without and with ZnO seed layer using Haacke's criteria as mentioned below:

$$\phi_H = \frac{T^{10}}{R_s} \tag{1}$$

Where, T and Rs are the optical transmittance measured at 550 nm and sheet resistance of the thin film, respectively. FOM measures the quality of deposited thin film to fulfill the criterion of being a high performance TCO. The higher value of FOM depicts the better quality of TCO thin films. In the present study, FOM has been calculated and found to be $2.72 \times 10^{-3}\ \Omega^{-1}$ and $1.68 \times 10^{-2}\ \Omega^{-1}$ for AZO-1 and AZO-2, respectively. ZnO seed layer assisted AZO thin film showed FOM higher than the other previous report on AZO thin films and TCO/metal/TCO structure [29–32].

The electrical conductivity and FOM for previously reported AZO thin film are compared with the present data and the results are shown in Table 2.

To know about the structural orientations of deposited AZO thin films, X-ray diffraction is performed over AZO-1 and AZO-2 and XRD pattern of the samples are shown in Fig. 4(a). Both AZO-1 and AZO-2 showed highly polycrystalline nature and (100), (221), and (002) peaks were found. The (001) and (002) peaks correspond to the ZnO wurtzite structure (JCPDS #36–1451). The (002) peak showed high intensity as compared to (100) peak. A shift of (100) and (002) peaks towards lower 2θ was observed that depicts the presence of residual stress in the AZO thin films (Figs. 4(a) and (c)). The (100) and (002) peaks of AZO-1 are shifted more towards the lower value of 2θ than in AZO-2 indicating the presence of higher residual stress in AZO-1. In the XRD pattern of AZO thin films, a very small and broad peak at 32.79° corresponding to (221) plane of the Al_2O_3 phase is also observed (JCPDS #46–1215). This peak suggests the segregation of a small amount of the Al_2O_3 phase in AZO thin films. However, no peak shift of (221) peak is observed for the Al_2O_3 phase in the AZO thin films. The reason for the formation of the Al_2O_3 phase may be attributed to the deposition of AZO thin film at high temperature that leads the segregation of extra Al in AZO to form the Al_2O_3 phase. The study also signified that an optimum composition of Al is required to achieve high optoelectronic properties in AZO thin film. In the present study, the phase segregation of Al_2O_3 in AZO thin film indicates that standard 2 wt% composition of Al_2O_3 in ZnO to improve the optoelectronic properties of ZnO may not be optimum. The average crystallite size of AZO thin films without and with ZnO seed layer was calculated using standard Scherrer formula:

$$L = \frac{0.9\lambda}{\beta cos\theta} \tag{2}$$

Where λ, θ and β are X-ray wavelength, the Bragg's diffraction angle and full width at half maxima of the peak corresponding to the θ, respectively.

The average crystallite size for peak (100) for AZO-1 and AZO-2 was calculated ~23 and ~22 nm, respectively. Similarly, the average crystallite size for peak (002) for AZO-1 and AZO-2 was calculated ~21 and ~20 nm, respectively.

The surface morphology scan of AZO-1 and AZO-2 thin films is carried out using AFM. The surface topography of AZO-1 and AZO-2 has measured over a 1 μm × 1 μm scan area and shown in Fig. 5. It is clearly observed from Figs. 5(a) and (b) that the surface topography of AZO-1 shows a large granular structure in the entire scan region while the surface topography of AZO-2 consists of small granular structures.

The difference in granular size may be interpreted using different initial growth mechanisms and the impact of the seed layer during the growth of AZO thin film. The surface line profile of AZO-1 and AZO-2 is shown in Figs. 5(c) and (d), respectively. The surface line profile is

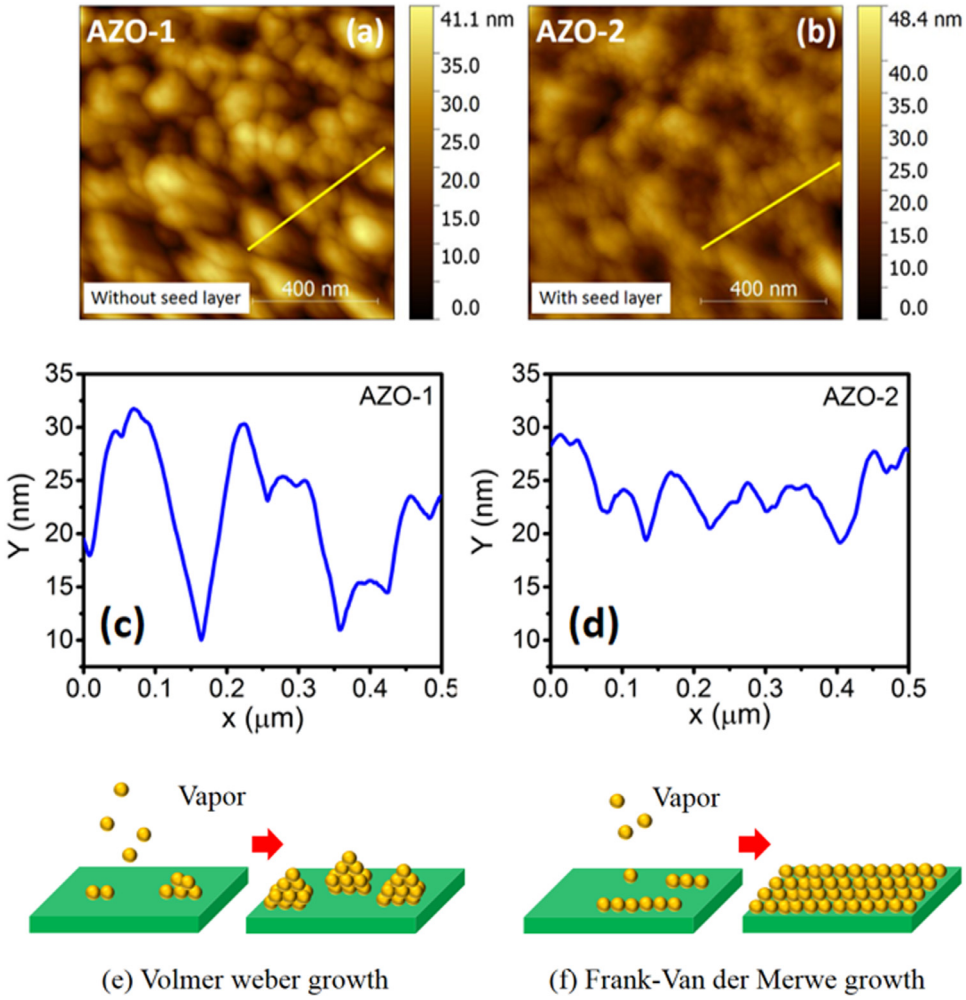

Fig. 5. Surface topography of AZO thin film deposited (a) without the ZnO seed layer and (b) with the ZnO seed layer. Line profile of AZO thin film taken over the yellow line drawn on the surface topography of AZO thin film deposited (c) without the ZnO seed layer and (d) with the ZnO seed layer. (e) and (f) show the schematic of the Volmer Weber growth and the Frank–Van der Merwe growth mechanism, respectively. The topography scan was performed over a 1 μm × 1 μm scan area.

taken over the yellow line drawn on the surface topography of AZO-1 and AZO-2, respectively. Figs. 5(c) and (d) also confirm the large granular size in AZO thin film deposited without the ZnO seed layer and smaller granular size in AZO thin film deposited with the ZnO seed layer. The AZO thin film deposited on the corning glass without the ZnO seed layer may have weak interaction with incoming sputtered AZO adatoms and glass substrate surface. This weak interaction might have initiated the island like growth (Volmer–Weber growth) and led a bigger granular size structure as shown by Fig. 5(a) and schematically shown in Fig. 5(e). On the contrary, in the case of the ZnO seed-layer assisted growth, incoming AZO adatoms have nearly the same surface energy as of the ZnO seed layer and adatoms have high interactions with seed-layer. Hence, this strong interaction between ZnO and AZO adatoms might have preferred the layer-by-layer like growth (Frank Van de Merwe) as shown by Figs. 5(b) and (f). Therefore, the growth model explains very well our surface topography of AZO-1 and AZO-2 thin films.

To understand the origin of high mobility in AZO thin film deposited with the ZnO seed layer (AZO-2), nanoscale Kelvin Probe Force Microscopy was performed. The KPFM images and variation of contact potential difference (surface potential) with respect to the lateral scale is shown in Figs. 6(b) and (d). The contact surface potential is measured along the yellow dashed line drawn on the KPFM images. The contact potential difference (CPD) is measured at different sites from peak to valley and average is taken out to give the qualitative magnitude of surface potential in AZO thin film grown without and with the ZnO seed layer.

Surface potential can depict the grain boundary potential that is formed by the segregation of free carried defects and get accumulated at the grain boundaries [23,44]. These defects accumulation form a surface charge layer and build a potential barrier that acts as a scattering barrier for free electrons in AZO thin film. The average surface potential of 122 ± ± 8.9 mV for AZO-1 while 93 ± 7.2 mV for AZO-2 thin film is observed. From KPFM results, it can be interpreted that low potential barrier in AZO-2 thin film is responsible for reduced carrier scattering and enhanced Hall mobility. Hence, the ZnO seed layer played a crucial role in reducing the grain boundary potential by reducing the free carrier defects density in the AZO thin film. Yildiz et al. also calculated the potential barrier at grain boundaries using Arrhenius plot for different dopants like Al, In, and Sn in ZnO matrix and showed the dependence of electrical properties and figure of merit on the grain boundaries potential [45]. McKenna et al. showed theoretically that the segregation of point defects towards the grain boundaries causes accumulation of defects and generation of space charge across the grain boundaries [44]. The accumulation of defects across grain boundaries may tend to arise potential fluctuations at grain boundaries and therefore, the electron transport properties can be limited by the potential barrier across the grain boundaries [46].

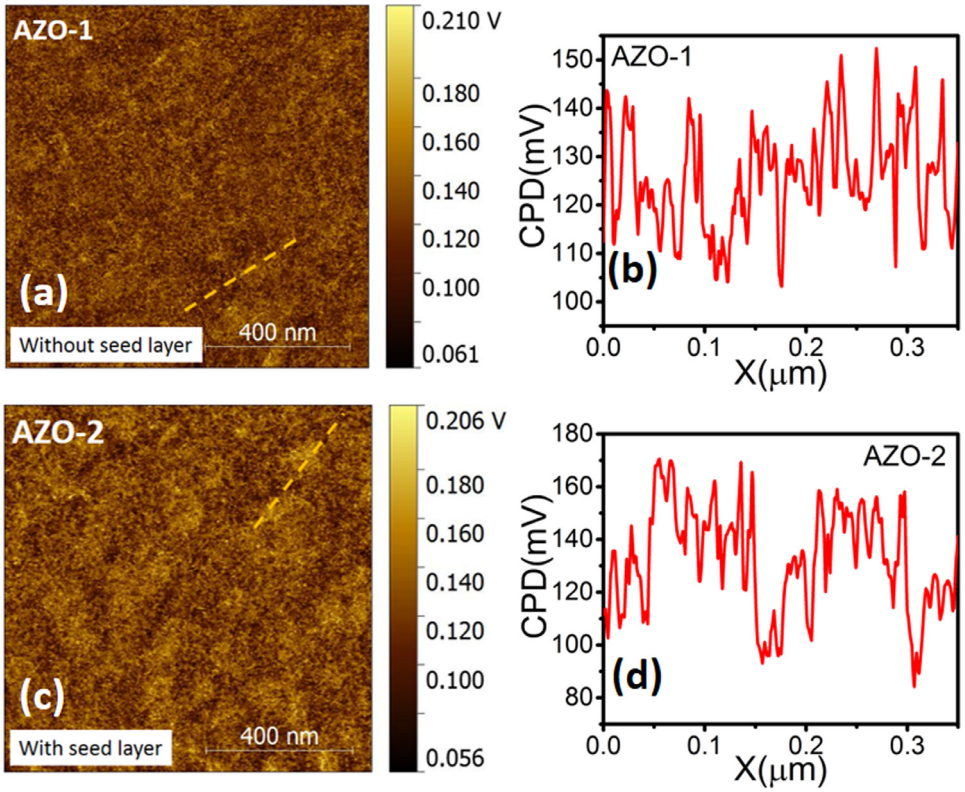

Fig. 6. (a) and (c) are the Kelvin Probe Force Microscopy (KPFM) of AZO thin film without and with the ZnO seed layer. (b) and (d) are the line profile of surface potential at mentioned locations in (a) and (c) profile, respectively.

To experimentally validate the low potential barrier due to the low defects segregation at grain boundaries in seed layer assisted grown AZO thin film, Conducting Atomic Force Microscopy and X-ray photoelectron spectroscopy are performed on AZO-1 and AZO-2 samples. For CAFM measurement Cr/Pt coated Si tip is used to measure the in the plane surface current. The substrate is biased at −4 V. Since the work function of AZO thin film and tip are 4.85 eV and 5.00 eV, respectively so under the current biasing condition the electron will flow towards the tip upon the biasing of the sample. The current measured will be due to the majority carrier in AZO thin film i.e. electrons. Fig. 7 shows the CAFM images and the surface current profile vs lateral distance where Figs. 7(a) and (c) are the CAFM images and Figs. 7(b) and (d) are the surface current profile taken along the yellow dashed line.

It is clearly evident from Figs. 7(a) and (c) that the surface current is much uniformly distributed in AZO-2 thin films as compared to AZO-1 thin films, respectively. Figs. 7(b) and (d) are the surface current profile taken for the yellow dashed line drawn on Figs. 7(a) and (c), respectively. The uniformity of surface current in AZO-2 can be interpreted as the presence of less number of defects that leads to the uninterrupted flow of carriers. On the application of biasing at the substrate, the free electrons will experience an electrostatic force that will drive them to recombine/trapped with the free carrier defects and the current uniformity detected by the CAFM measurements will be highly affected.

Fig. 8 shows the schematic of CAFM measurements. The CAFM image of AZO-1 showed the poor uniformity of surface current in contrast to AZO-2. The poor uniformity of surface current in AZO-1 may be attributed to the presence of a higher number of defects than in AZO-2 thin film with the ZnO seed layer. Therefore, the lesser number of defects in AZO-2, as suggested by the CAFM measurements forms a low potential barrier of electrons and contributes to the high carrier mobility. The schematic view of the recombination of electrons with traps states in AZO thin film deposited without and with the ZnO seed layer is shown in Fig. 8. Fig. 8 depicts the higher trap states in AZO thin film deposited without the ZnO seed layer than AZO thin film deposited with the ZnO seed layer. The presence of higher traps states in AZO-1 gives less uniform surface current as compared to AZO-2. Therefore, Fig. 8 helps us to understand the uniformity of surface current and nanoscale distribution of trap states formed by the defects in both AZO-1 and AZO-2 thin films. Likovich et al. also demonstrated the accumulation of trap states near grain boundaries using scanning tunneling microscopy in AZO and showed their impact on electrical properties due to the formation of potential barriers [47].

To study more profoundly about the defects and their nature in AZO thin films, X-ray photoelectron spectroscopy was carried out over the AZO thin films. The carbon correction has been done using an adventitious carbon C1s peak present at 284.8 eV.

The O1s peak of AZO-1 and AZO-2 is deconvoluted into three O_I, O_{II} and O_{III} sub-peaks (Figs. 9(a) and (b)). The O_I, O_{II}, and O_{III} peaks present around 530.45 eV, 530.96 eV and 532.10 eV correspond to the O^{2-} ions bonded to the Zn^{2+} in the wurtzite structure of hexagon array of the ZnO, oxygen vacancies in the Zn-O matrix and loosely bound chemisorbed oxygen, respectively [23,48–50]. Therefore, any variation in the area of O_{II} peak is directly correlated to the concentration of oxygen vacancies in the AZO thin films [49,51,52].

To get the qualitative information about oxygen vacancies, the ratio $O_{II}/(O_I+O_{II}+O_{III})$ was calculated and shown in Table 3. The ratio was found 0.63 for AZO-1 and 0.53 for AZO-2 that depicts the low oxygen vacancies (point defects) in AZO-2 thin films. Since, free carries defects migrate towards the grain boundaries and develop a surface charge layer and form grain boundary potential [23,44]. Therefore, the low value of $O_{II}/(O_I+O_{II}+O_{III})$ ratio for AZO-2 suggests low oxygen vacancies that may be responsible for low grain boundaries potential.

Similarly, to get the information about zinc related defects, the Zn 2P 3/2 peak also deconvoluted into Zinc interstitials (Zn_i) peak and Zinc bonded to oxygen peak in the ZnO matrix (Zn-O). The peak at 1021.35 eV and 1022.2 eV correspond to the Zn_i and Zn-O peak, respectively that give the qualitative information about the zinc interstitials (metallic zinc) and zinc bonded to oxygen in ZnO matrix,

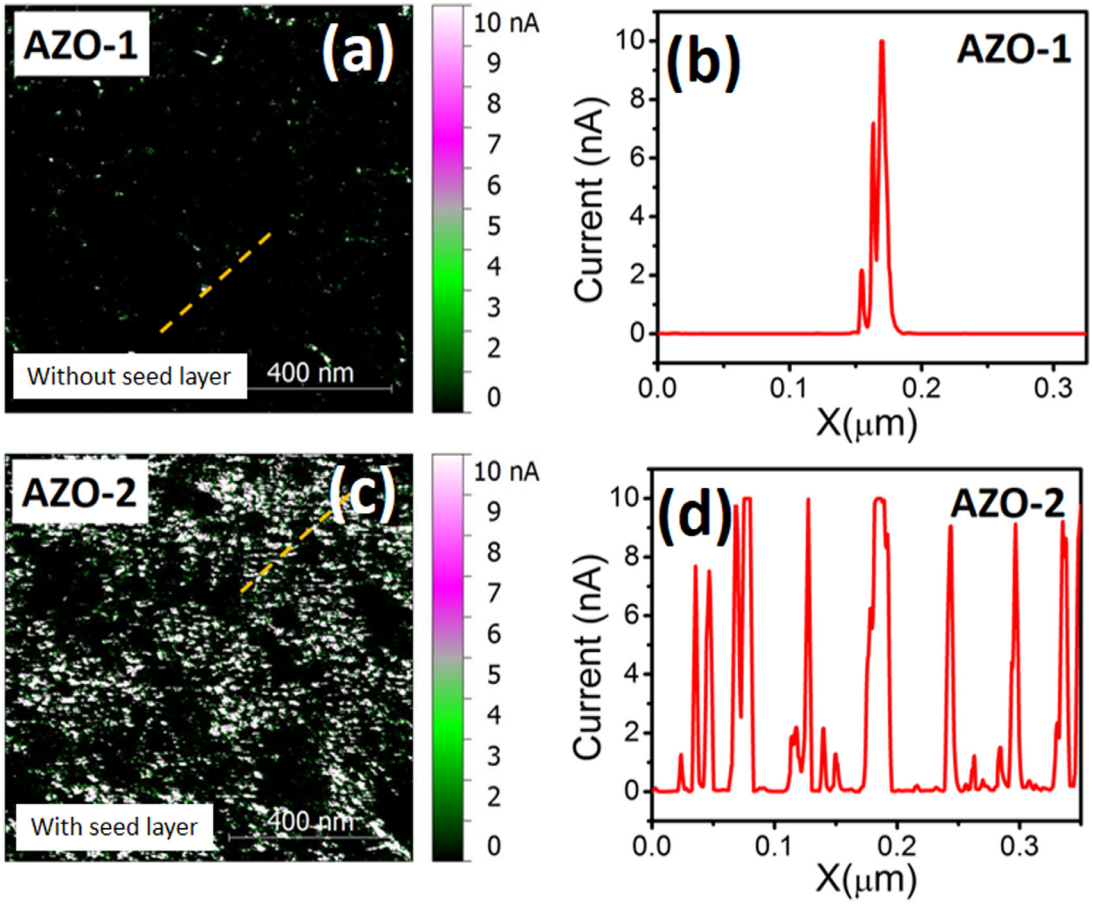

Fig 7. (a) and (c) are the CAFM images of AZO thin film without the ZnO seed layer and with the ZnO seed layer. (b) and (d) are the surface current vs. lateral scan profile taken for the yellow dashed line drawn on the (a) and (c) profile, respectively.

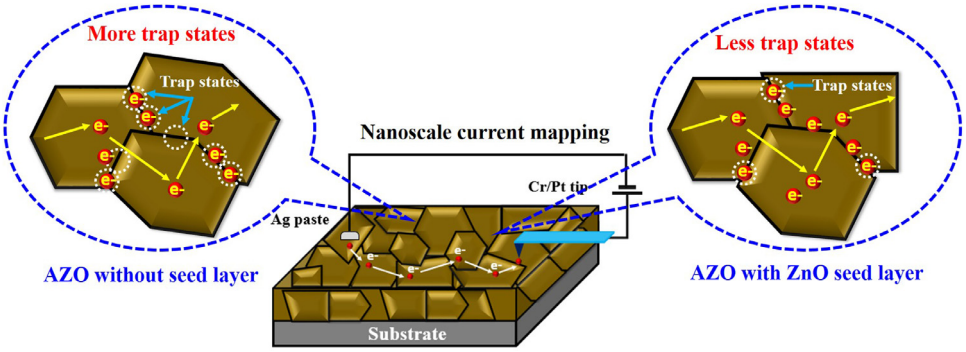

Fig. 8. Schematic diagram of CAFM measurement of the ZnO seed layer assisted AZO thin film where the substrate is biased. Zoom out view of CAFM measurement shows the recombination of electron-hole pair due to the defects states present near the grain boundaries.

respectively [48–50]. Figs. 9(c) and (d) show the deconvoluted XPS spectra of Zn 2P 3/2 peak of AZO-1 and AZO-2, respectively.

It is evident from Figs. 9(c) and (d) and table 4 that AZO-1 contains high zinc interstitials (other zinc related defects) than AZO-2. The large area of Zn_i peak of AZO-1 is clearly an indication of the presence of a large number of Zinc interstitials that may form defects states.

Therefore, on summarizing the XPS analysis of AZO-1 and AZO-2, large oxygen related defects and zinc related defects were shown by the AZO-1 thin film and these defects may be migrated towards the grain boundaries to build up a high grain boundary potential as compared to AZO-2 that exhibited less free defects states and small potential barrier. The XPS analysis also supports and validates the argument of low free defects suggested by the CAFM measurements for AZO-2 thin films.

In order to understand the origin of an increase in carrier density in ZnO seed layer assisted grown AZO thin film, the XPS spectra of Al 2p of AZO-1 and AZO-2 is also deconvoluted into two peaks (Figs. 9(e) and (f)). The green peak around 74.7 eV corresponds to the substitution of Al into Zn^{2+} sites of the ZnO matrix and confirms the formation of the AZO phase [48,53]. The pink peak that lies around 73.6 eV, in between 72.7 eV (metallic Al) and 74.7 eV (AZO) is attributed to the formation of non-stoichiometric of Al_xO_y. Therefore, it may be concluded that Al atoms substitute for Zn atoms in AZO thin film and forms a non-stoichiometric complex which after heat treatment can act as an Al donor [37]. It is notably apparent from the comparison of Figs. 9(e) and (f) that the area of pink peak is higher in AZO-2 than AZO-1 which subsequently gives to AZO-2 an increased carrier density. Moreover, the

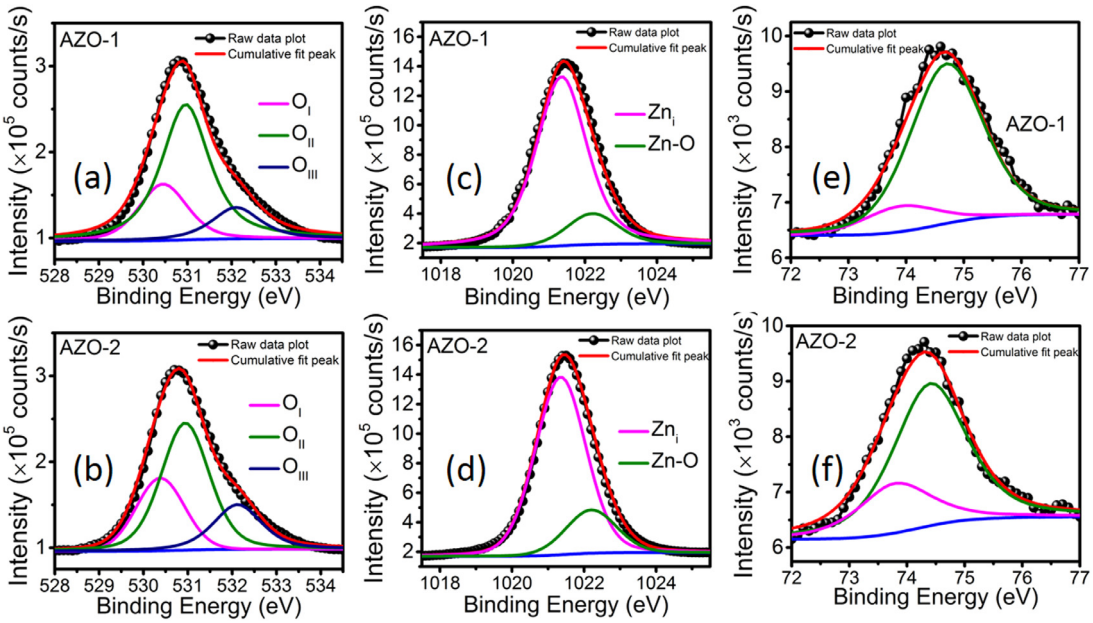

Fig. 9. XPS spectra of O 1 s peak of (a) AZO thin film without the ZnO seed layer (AZO-1) and (b) AZO thin film with the ZnO seed layer (AZO-2). XPS spectra of Zn 2P peak of (c) AZO thin film without the ZnO seed layer (AZO-1) and (d) AZO thin film with the ZnO seed layer (AZO-2). The Al 2p XPS spectra of (e) AZO thin film deposited without the ZnO seed layer (AZO-1) and (f) AZO thin film deposited with the ZnO seed layer (AZO-2).

Table 3
Peak position and area of OI, OII, and OIII peaks are shown and OII/(OI + OII + OIII) is also calculated to quantify the oxygen vacancies.

Sample name	Peak Position O_I	Area O_I	Peak Position O_{II}	Area O_{II}	Peak Position O_{III}	Area O_{III}	$O_{II}/(O_I+O_{II}+O_{III})$
AZO-1	530.45	105,718.5	530.96	287,203.9	532.10	65,458.03	0.63
AZO-2	530.38	118,090.1	530.94	230,671.0	532.12	88,079.49	0.53

Table 4
Peak position and area of Zn 2P deconvoluted into Zn interstitials (Zni) peak and zinc bonded to oxygen (Zn-O).

Sample name	Peak Position Zn_i	Area Zni	Peak Position Zn-O	Area Zn-O
AZO-1	1021.35	2,450,009	1022.2	412,214.6
AZO-2	1021.35	2,273,272	1022.2	543,636.6

area of green peak is lesser in AZO-2 than AZO-1 that may be interpreted as the formation of more Al_xO_y non-stoichiometric complex than Al atoms substitution at Zn^{2+} sites in the ZnO matrix. The analysis of Al 2P XPS spectra elucidates the origin of high carrier density in the ZnO seed layer assisted AZO thin film.

The present work has elucidated the importance of free carrier defects in controlling the carrier mobility and origin of enhanced carrier mobility in the ZnO seed layer grown AZO thin film. Nanoscale carrier transport and nanoscale defect distribution also showed that the seed layer controls the defects in the AZO thin films and improves the optoelectronic properties.

4. Conclusions

AZO thin film deposited with the ZnO seed layer showed an almost two-fold increase in carrier mobility and high electrical conductivity than AZO thin film grown without the ZnO seed layer. Both AZO thin films without and with the ZnO seed layer showed highly polycrystalline nature. To understand the origin of enhanced carrier mobility and electrical conductivity in the ZnO seed layer assisted AZO thin films, KPFM was performed that showed low grain boundary potential for the ZnO seed layer grown AZO thin films and high grain boundary potential for AZO film deposited without ZnO seed layer. The low grain boundary potential in the ZnO seed layer assisted AZO thin film was attributed to the presence of low zinc and oxygen related defects than AZO thin film deposited without the ZnO seed layer. The low defects argument in the ZnO seed layer grown AZO thin film was validated by the nanoscale current mapping and nature of defects generated in AZO thin films. The nanoscale surface current mapping in both the AZO thin films showed nanoscale defects distribution and recombination of free carriers.

Author contribution section

Authors	Contribution
Naveen Kumar and Mukesh Kumar	Identification of problem, execution, data analysis, and manuscript writing
Ashraful Haider Chowdhury Behzad Bahrami Khan Mamun Reza Qiquan Qiao	Performed XRD, AFM, CAFM, and KPFM measurements. Check the manuscript.

Declaration of Competing Interests

None.

Acknowledgement

Author sincerely acknowledges the department of physics, IIT Ropar

for SEED grant and funding through the interdisciplinary Solar PV project from Indian Institute of Technology Ropar.

References

[1] R.M. Pasquarelli, D.S. Ginley, R. O'Hayre, Solution processing of transparent conductors: from flask to film, Chem. Soc. Rev. 40 (2011) 5406–5441.
[2] S.C. Dixon, D.O. Scanlon, C.J. Carmalt, I.P. Parkin, n-Type doped transparent conducting binary oxides: an overview, J. Mater. Chem. C 4 (2016) 6946–6961.
[3] S. Calnan, A.N. Tiwari, High mobility transparent conducting oxides for thin film solar cells, Thin Solid Films 518 (2010) 1839–1849.
[4] Q. Qiao, J. Beck, R. Lumpkin, J. Pretko, J.T. McLeskey, A comparison of fluorine tin oxide and indium tin oxide as the transparent electrode for P3OT/TiO2 solar cells, Sol. Energ. Mat. Sol. C 90 (2006) 1034–1040.
[5] B.-.Y. Oh, M.-.C. Jeong, T.-.H. Moon, W. Lee, J.-.M. Myoung, J.-.Y. Hwang, D.-.S. Seo, Transparent conductive Al-doped ZnO films for liquid crystal displays, J. Appl. Phys. 99 (2006) 124505.
[6] S.H. Sabeeh, R.H. Jassam, The effect of annealing temperature and Al dopant on characterization of ZnO thin films prepared by sol-gel method, Results Phys. 10 (2018) 212–216.
[7] S. Takaki, K. Matsumoto, K. Suzuki, Properties of highly conducting ITO films prepared by ion plating, Appl. Surf. Sci. 33-34 (1988) 919–925.
[8] F.L. Wong, M.K. Fung, S.W. Tong, C.S. Lee, S.T. Lee, Flexible organic light-emitting device based on magnetron sputtered indium-tin-oxide on plastic substrate, Thin Solid Films 466 (2004) 225–230.
[9] D.S. Ginley, C. Bright, Transparent conducting oxides, MRS Bull. 25 (2011) 15–18.
[10] Z. Chen, W. Li, R. Li, Y. Zhang, G. Xu, H. Cheng, Fabrication of highly transparent and conductive indium–tin oxide thin films with a high figure of merit via solution processing, Langmuir 29 (2013) 13836–13842.
[11] M.C. Jun, S.U. Park, J.H. Koh, Comparative studies of Al-doped ZnO and Ga-doped ZnO transparent conducting oxide thin films, Nanoscale Res. Lett. 7 (2012) 639.
[12] J.W. Leem, J.S. Yu, Structural, optical, and electrical properties of AZO films by tilted angle sputtering method, Thin Solid Films 518 (2010) 6285–6288.
[13] N. Tsukamoto, D. Watanabe, M. Saito, Y. Sato, N. Oka, Y. Shigesato, In situ analyses on negative ions in the sputtering process to deposit Al-doped ZnO films, J. Vac. Sci. Technol. A 28 (2010) 846–850.
[14] T.T.T. Vo, K.P.O. Mahesh, P.-.H. Lin, Y. Tai, Impact of self-assembled monolayer assisted surface dipole modulation of PET substrate on the quality of RF-sputtered AZO film, Appl. Surf. Sci. 403 (2017) 356–361.
[15] Z.-.L. Tseng, P.-.C. Kao, Y.-.C. Chen, Y.-.D. Juang, Y.-.M. Kuo, S.-.Y. Chu, Effect of thicknesses on the structure, conductivity, and transparency of Al-doped ZnO anodes in organic light-emitting diodes, J. Electrochem. Soc. 158 (2011) J310–J315.
[16] N. Ito, N. Oka, Y. Sato, Y. Shigesato, Effects of energetic ion bombardment on structural and electrical properties of al-doped ZnO films deposited by RF-Superimposed DC magnetron sputtering, Jpn. J. Appl. Phys. 49 (2010) 071103.
[17] H.-.S. Kim, S.H. Jeon, J.S. Park, T.S. Kim, K.S. Son, J.-.B. Seon, S.-.J. Seo, S.-.J. Kim, E. Lee, J.G. Chung, H. Lee, S. Han, M. Ryu, S.Y. Lee, K. Kim, Anion control as a strategy to achieve high-mobility and high-stability oxide thin-film transistors, Sci. Rep. 3 (2013) 1459.
[18] J. Nomoto, H. Makino, T. Yamamoto, Carrier mobility of highly transparent conductive Al-doped ZnO polycrystalline films deposited by radio-frequency, direct-current, and radio-frequency-superimposed direct-current magnetron sputtering: grain boundary effect and scattering in the grain bulk, J. Appl. Phys. 117 (2015) 045304.
[19] F. Wang, M.Z. Wu, Y.Y. Wang, Y.M. Yu, X.M. Wu, L.J. Zhuge, Influence of thickness and annealing temperature on the electrical, optical and structural properties of AZO thin films, Vacuum 89 (2013) 127–131.
[20] H. Tanaka, K. Ihara, T. Miyata, H. Sato, T. Minami, Low, resistivity polycrystalline ZnO:Al thin films prepared by pulsed laser deposition, J. Vac. Sci. Technol. A 22 (2004) 1757–1762.
[21] B.-.Z. Dong, G.-.J. Fang, J.-.F. Wang, W.-.J. Guan, X.-.Z. Zhao, Effect of thickness on structural, electrical, and optical properties of ZnO: Al films deposited by pulsed laser deposition, J. Appl. Phys. 101 (2007) 033713.
[22] C. Singh, E. Panda, Variation of electrical properties in thickening Al-doped ZnO films: role of defect chemistry, Rsc. Adv. 6 (2016) 48910–48918.
[23] N. Kumar, A. Dubey, B. Bahrami, S. Venkatesan, Q. Qiao, M. Kumar, Origin of high carrier mobility and low residual stress in RF superimposed DC sputtered Al doped ZnO thin film for next generation flexible devices, Appl. Surf. Sci. 436 (2018) 477–485.
[24] M. Kumar, A.K. Sigdel, T. Gennett, J.J. Berry, J.D. Perkins, D.S. Ginley, C.E. Packard, Optimizing amorphous indium zinc oxide film growth for low residual stress and high electrical conductivity, Appl. Surf. Sci. 283 (2013) 65–73.
[25] M. Bender, J. Trube, J. Stollenwerk, Deposition of transparent and conducting indium-tin-oxide films by the r.f.-superimposed DC sputtering technology, Thin Solid Films 354 (1999) 100–105.
[26] N. Yamamoto, H. Makino, T. Yamada, Y. Hirashima, H. Iwaoka, T. Ito, A. Ujihara, H. Hokari, H. Morita, T. Yamamoto, Heat resistance of Ga-doped ZnO thin films for application as transparent electrodes in liquid crystal displays, J. Electrochem. Soc. 157 (2010) J13–J20.
[27] N. Kumar, T.M. Wilkinson, C.E. Packard, M. Kumar, Design of low surface roughness-low residual stress-high optoelectronic merit a-IZO thin films for flexible OLEDs, J. Appl. Phys. 119 (2016) 225303.
[28] K. Arora, N. Goel, M. Kumar, M. Kumar, Ultrahigh performance of self-powered β-Ga2O3 thin film solar-blind photodetector grown on cost-effective Si substrate using high-temperature seed layer, ACS Photonics 5 (2018) 2391–2401.
[29] K.N. Tonny, R. Rafique, A. Sharmin, M.S. Bashar, Z.H. Mahmood, Electrical, optical and structural properties of transparent conducting Al doped ZnO (AZO) deposited by sol-gel spin coating, AIP Adv. 8 (2018) 065307.
[30] M.C. Jun, J.H. Koh, Effects of NIR annealing on the characteristics of al-doped ZnO thin films prepared by RF sputtering, Nanoscale Res. Lett. 7 (2012) 294.
[31] A. Bahadoran, N. Zare-Dehnavi, The Ag layer thickness effect on the figure of merit of the AZO/Ag bilayer prepared by DC sputtering of AZO and thermal evaporation method of Ag, Mater. Res. Express 6 (2018) 026406.
[32] C. Bhoomanee, P. Ruankham, S. Choopun, D. Wongratanaphisan, Diffusion-induced doping effects of Ga in ZnO/Ga/ZnO and AZO/Ga/AZO multilayer thin films, Appl. Surf. Sci. 474 (2019) 127–134.
[33] J.B. Kim, S.B. Jin, L. Wen, P. Premphet, K. Leksakul, J.G. Han, Low temperature, high conductivity Al-doped ZnO film fabrication using modified facing target sputtering, Thin Solid Films 587 (2015) 88–93.
[34] D.K. Kim, H.B. Kim, Room temperature deposition of Al-doped ZnO thin films on glass by RF magnetron sputtering under different Ar gas pressure, J. Alloy. Compd. 509 (2011) 421–425.
[35] T. Yang, S. Song, Y. Li, Y. Xin, G. Du, M. Lv, S. Han, The enhanced conductivity and stability of AzO thin films with a TiO2 buffer layer, Physica B 407 (2012) 4518–4522.
[36] P. Sagar, M. Kumar, R.M. Mehra, Influence of hydrogen incorporation in sol-gel derived aluminum doped ZnO thin films, Thin Solid Films 489 (2005) 94–98.
[37] P.-.C. Yao, S.-.T. Hang, Y.-.S. Lin, W.-.T. Yen, Y.-.C. Lin, Optical and electrical characteristics of Al-doped ZnO thin films prepared by aqueous phase deposition, Appl. Surf. Sci. 257 (2010) 1441–1448.
[38] Y.-.S. Liu, C.-.Y. Hsieh, Y.-.J. Wu, Y.-.S. Wei, P.-.M. Lee, H.-.M. Hsieh, C.-.Y. Liu, Mechanism of conductivity degradation of AzO thin film in high humidity ambient, Appl. Surf. Sci. 282 (2013) 32–37.
[39] Z.P. Kan, Z.W. Wang, Y. Firdaus, M. Babics, H.N. Alshareef, P.M. Beaujuge, Atomic-layer-deposited AzO outperforms ITO in high-efficiency polymer solar cells, J. Mater. Chem. A 6 (2018) 10176–10183.
[40] R.N. Chauhan, N. Tiwari, R.S. Anand, J. Kumar, Development of Al-doped ZnO thin film as a transparent cathode and anode for application in transparent organic light-emitting diodes, Rsc. Adv. 6 (2016) 86770–86781.
[41] R.C. Raju Nagiri, S.D. Yambem, Q. Lin, P.L. Burn, P. Meredith, Room-temperature tilted-target sputtering deposition of highly transparent and low sheet resistance Al doped ZnO electrodes, J. Mater. Chem. C 3 (2015) 5322–5331.
[42] I. Crupi, S. Boscarino, V. Strano, S. Mirabella, F. Simone, A. Terrasi, Optimization of ZnO:Al/Ag/ZnO:Al structures for ultra-thin high-performance transparent conductive electrodes, Thin Solid Films 520 (2012) 4432–4435.
[43] Q. Xu, W. Shen, Q. Huang, Y. Yang, R. Tan, K. Zhu, N. Dai, W. Song, Flexible transparent conductive films on PET substrates with an AZO/AgNW/AZO sandwich structure, J. Mater. Chem. C 2 (2014) 3750–3755.
[44] K.P. McKenna, A.L. Shluger, First-principles calculations of defects near a grain boundary in MgO, Phys. Rev. B 79 (2009) 224116.
[45] A. Yildiz, S. Uzun, N. Serin, T. Serin, Influence of grain boundaries on the figure of merit of undoped and Al, In, Sn doped ZnO thin films for photovoltaic applications, Scr. Mater. 113 (2016) 23–26.
[46] J. Werner, Electronic Properties of Grain Boundaries, Springer, Berlin Heidelberg, 1985, pp. 76–94 Berlin, Heidelberg.
[47] E.M. Likovich, R. Jaramillo, K.J. Russell, S. Ramanathan, V. Narayanamurti, Scanning tunneling microscope investigation of local density of states in Al-doped ZnO thin films, Phys. Rev. B 83 (2011) 075430.
[48] J. Wang, Y. Li, Y. Kong, J. Zhou, J. Wu, X. Wu, W. Qin, Z. Jiao, L. Jiang, Non-fluorinated superhydrophobic and micro/nano hierarchical Al doped ZnO film: the effect of Al doping on morphological and hydrophobic properties, Rsc. Adv. 5 (2015) 81024–81029.
[49] M. Chen, Z.L. Pei, C. Sun, L.S. Wen, X. Wang, Formation of Al-doped ZnO films by dc magnetron reactive sputtering, Mater. Lett. 48 (2001) 194–198.
[50] S. Sharma, R. Bayikadi, P. Swaminathan, Spark plasma sintering route to synthesize aluminium doped zinc oxide, Rsc. Adv. 6 (2016) 86586–86596.
[51] M. Chen, X. Wang, Y.H. Yu, Z.L. Pei, X.D. Bai, C. Sun, R.F. Huang, L.S. Wen, X-ray photoelectron spectroscopy and auger electron spectroscopy studies of Al-doped ZnO films, Appl. Surf. Sci. 158 (2000) 134–140.
[52] J.C.C. Fan, J.B. Goodenough, X-ray photoemission spectroscopy studies of Sn-doped indium-oxide films, J. Appl. Phys. 48 (1977) 3524–3531.
[53] R. Sankar ganesh, M. Navaneethan, G.K. Mani, S. Ponnusamy, K. Tsuchiya, C. Muthamizhchelvan, S. Kawasaki, Y. Hayakawa, Influence of Al doping on the structural, morphological, optical, and gas sensing properties of ZnO nanorods, J. Alloy Compd. 698 (2017) 555–564.